X-ray Diffraction Reveals Periodicity in Murine Neocortex

Sasha Murokh[1,2], Ezekiel Willerson[3,4], Alexander Lazarev[5], Pavel Lazarev[2,5], and Joshua Brumberg[3,4,*]

[1] Stuyvesant High School, 345 Chambers Street, New York, NY 10282, USA
[2] Matur UK Ltd., 5 New Street Square, London EC4A 3TW, UK
[3] Department of Psychology, Queens College of the City University of New York, 65-30 Kissena Blvd, Flushing, NY 11367, USA
[4] Graduate Center of the City University of New York, 365 5th Ave, New York, NY 10016, USA
[5] Arion Diagnostics, Inc., 911 Mustang Ct, Petaluma, CA 94954, USA

*Corresponding Author :
Joshua C. Brumberg
Department of Psychology
Queens College, CUNY
65-30 Kissena Boulevard
Flushing, NY 11367, USA
Email : Joshua.brumberg@qc.cuny.edu
Phone : (718) 997-3541

Keywords: Perineuronal net, x-ray diffraction, barrel cortex, sensory deprivation

Words in Abstract: 185
Figures: 4
Tables: 1

Abstract

Background: The perineuronal net (PNN) is a form of extracellular matrix which develops as a lattice-like structure around neuronal somas, proximal dendrites and synapses. In homeostasis, it supports synaptic stability, protects neurons, and helps regulate inhibition/excitation. In pathology, it has been described as degraded or even absent. Sensory deprivation has been shown to alter PNN structures.

New Methods: Here, we measured the X-ray diffraction patterns of mouse brain tissue to establish a novel method for examining nanoscale brain structures. Two groups of mice were examined, a control group, and one which underwent 30 days (P0-P30) of whisker-trimming – an established method of sensory deprivation, affecting the mouse barrel cortex (whisker sensory processing region of somatosensory cortex). Mice were perfused, and primary somatosensory cortices (barrel cortex) were isolated for x-ray diffraction imaging.

Results: X-ray images were characterized using a specially developed machine-learning approach, and the clusters that correspond to the two groups are well separated in the space of the principal components.

Conclusions: We hypothesize that such separation is related to the development of nanoscale structural components within PNNs of control mice and the absence of such structures in sensory deprived mice.

1. Introduction

X-ray absorption has been widely used in medicine since its discovery. However, another effect, X-ray diffraction (or, more generally, scattering), has not been implemented widely. Initially, it was utilized for X-ray crystallography, determining the atom arrangements in crystalline solids (Bragg, 1914). Later, bio-crystallography based on crystallized biological molecules facilitated the revealing of the molecular content of complex structures, including myoglobin, hemoglobin, and DNA; see (Shi, 2014; Higgins & Lea, 2017) for historical overviews. However, the X-ray scattering approach can be applied directly to biological tissues, and if there are periodic structures, they will manifest themselves in characteristic scattering patterns. In this, any periodicity, d, of the structure, such as regular intermolecular distances in molecular packing or the pitch in multiple-helix fibrils, will appear as momentum transfer, $q = 2\pi n/d$. In particular, the 64 nm pitch of the triple helix of collagen produces peaks in the X-ray scattering patterns at 0.1 nm^{-1} and its multiples (Worthington & Tomlin, 1955). Recently, X-ray scattering has been used to detect cancer-induced changes in the extracellular matrix, specifically in breast cancer applications (Kidane et al., 2017; Cunha et al., 2006; Conceicao et al., 2010; Conceicao et al., 2009; Denisov et al., 2024). It was reported that because of broken lipid metabolism in the tumor microenvironment, the peak at 1.5 nm^{-1}, associated with the triglyceride packing, disappears, and another peak, at 13.9 nm^{-1}, related to inter-fatty-acid molecular distances, is strongly suppressed. In this paper, we show for the first time that X-ray scattering can also be applied to brain tissues to examine their structural properties.

Perineuronal nets (PNNs) are lattice-like structures found in the extracellular matrix ensheathing neurons, comprised primarily of chondroitin sulphate proteoglycans (CSPGs) cross-hatched together via tenascin-R and bound to a hyaluronan backbone through linker proteins (Härtig et al., 1992). Within the cerebral cortex, these nets form barriers primarily around parvalbumin expressing (PV+) GABAergic interneurons and are key players in maintaining synaptic stability and protecting these neurons from damage (Crapser et al., 2020; Suttkus et al., 2016). PV+ interneurons are important for excitation/inhibition balance during excitatory input (Hijazi et al., 2023). In pathologies such as Alzheimer's, schizophrenia, and chronic pain, PNNs have been reported as degraded or significantly restructured in a region-specific manner (Crapser et al., 2020; Mauney et al., 2013; Tansley et al., 2022). Further, changes in sensory input or neuronal activity have been shown to alter PNN density, and sensory deprivation results in a reduction of PNNs in affected regions (Pizzorusso et al., 2002; McRae et al., 2007). Whisker-trimming in mice is one form of sensory deprivation which has been shown to affect PNN quantity. Both adult mice and newborn pups which undergo 30 days of whisker-trimming show significantly less PNN coverage in the barrel cortex – the region associated with whisker sensation processing – compared with untrimmed mice (McRae et al., 2007). Given this, PNNs have become a useful target for understanding neuronal changes occurring in the brain and provide a substrate to test the possibility of x-ray scattering utility in scanning biological tissue such as the cerebral cortex.

2. Methods

2.1. Animals and Trimming procedure:
Pregnant CD-1 mouse dams were ordered from Charles River to give birth in-facility. Mice were housed as dams plus pups for the duration of the experiment, with each litter serving as either the control or experimental group separately. Animals were housed in standard mouse cages and received *ad libitum* access to food and water. Experiments were in accordance with NIH standards for the use of animals for biomedical research and approved by the Queens College, City University of New York, Institutional Animal Care and Use Committee (protocol #208).

Sensory deprivation via whisker-trimming took place every other day from postnatal day (P) 0 (day of birth) to P29. For the experimental "trimmed whiskers" (TW) group, pups were briefly removed from their litter and whiskers were trimmed bilateral using Vanna scissors (F.S.T., Catalog #'s 15002-08 or 15018-10). Control group("untrimmed") pups were similarly removed from their litter, handled identically, and then returned to their home cage without trimming. From P0-P12 whisker-trimming and handling was performed on awake pups. From P13-P29 trimming and handling was done under light anesthesia to ensure proper trimming and reduce risk of injury to pups. Isoflurane (3% in room air) was administered for 30 second to 1 minute prior to trimming, resulting in the pups being lightly unconscious. Untrimmed control pups were also subjected to isoflurane. Pups were returned to their litter as they regained consciousness.

Mice were euthanized with an intraperitoneal injection (Euthasol, 100mg/kg) and perfused on P30. Deep anesthesia was confirmed when a toe pinch no longer elicited a paw withdrawal. Mice were perfused with 0.9% NaCl followed by 4% paraformaldehyde dissolved in 0.1M phosphate buffered saline (PBS). Following removal brain tissue was preserved in 4% paraformaldehyde in 0.1M PBS at 4ºC.

2.2. Staining for perineuronal nets:
For tissue staining, brains were submerged in 4%cparaformaldehyde in 0.1M PBS for 24 hours before being placed in a 30% sucrose solution for three days (or until sunk). The barrel cortex was located using an adult mouse brain atlas (Paxinos and Franklin's *The Mouse Brain in Stereotaxic Coordinates*, 5th edition, 2019) and sectioned at 16 µm on a freezing stage microtome (Epredia, HM450). For perineuronal net visualization, tissue sections were washed in 0.01M PBS (3 x 5 minutes) before submerging in a solution of 0.06% hydrogen peroxide combined with 1% methanol by volume in 0.01M PBS to quench endogenous peroxidase activity (30 minutes). Following three washes of 5 minutes in 0.01M PBS, free-floating tissue was further incubated in a solution of biotinylated wisteria floribunda agglutinin (Sigma-Aldrich, L1516-2MG; 1:500 ratio) with 2% normal goat serum dissolved in 0.01M PBS for 72 hours at 4ºC. After this initial incubation, tissue was rinsed again three times (5 minutes each) in 0.01M PBS before immersing in an avidin-biotin complex (ABC; Vector labs, PK-4000) in the same concentration PBS for 30 minutes. Following another three washes of 5 minutes each in 0.01M PBS the perineuronal nets were visualized by reacting the bound ABC with 3,3′-Diaminobenzidine tetrahydrochloride (Sigma-Aldrich, D5905; 2mg/mL PBS), nickel chloride (0.04%), and hydrogen peroxide (0.15%) solution dissolved in 0.01M PBS, brain slices were mounted and then allowed to dry on gelatinized glass slides for 24 hours. Gelatinized slides were prepared ahead of time by submerging slides in porcine gelatine (5g/1000mL water) with chromium potassium sulfate (0.5g). Tissue was then dehydrated and defatted by submerging slides in increasing

concentrations of ethanol (50%, 70%, 95%, 100%) before finally washing in Safeclear for 5 minutes (Fisher-Scientific, 314-629). Slides were coverslipped with Permount mounting medium (Fisher Chemical, SP15) and allowed to air dry prior to observation.

2.3. Sectioning for x-ray diffraction:

Tissue used for x-ray diffraction were from different animals and not sunk in sucrose but removed from the brain in the same way as the tissue utilized for immunocytochemistry. Left and right hemisphere barrel cortices were sectioned (described below) in their entirety for each subject. Using coordinates from the Paxinos and Franklin's mouse brain atlas (2019), the barrel cortex was determined to be 3.88 and 6.12 mm medially from the rostral and caudal ends of the brain (respectively). Initial cuts were made as closely to these measurements as possible, using 0.25 mm and 0.5 mm brain matrices (Zivic Instruments; Braintree Scientific) and a mm ruler. Mediolaterally, the barrel cortex was determined to span the region 2.25 to 4 mm laterally from the longitudinal fissure. The cortex was sectioned away from the underlying white matter just superior to the corpus callosum, with the cortical plate having a thickness of about 1 mm. Total isolated section size measured approximately 2.4 mm on the rostrocaudal axis, 1.75 mm mediolaterally, and 1 mm thick (isolated cortex). Post-sectioning, tissue was stored in 0.01M PBS at 4ºC, and experimenters performing x-ray diffraction were blinded to condition.

2.4. Quantification of Immunohistochemistry

Stained PNNs were quantified using luminance measurements embedded within the Neurolucida software (MBF Bioscience), which averages the brightness of each pixel in a defined region to create a "brightness" score. First, the barrel cortex was traced using the Paxinos and Franklin's atlas (2019) as a guide. Second, because very few PNNs exist in white matter, white matter local to each barrel cortex was also traced to be used as a comparison point for the barrel cortex. Third, white matter was imaged with lighting adjusted in intensity to normalize images to a 200 (+/- 4) brightness score. Fourth, the barrel cortex was imaged at the same light level. Lastly, brightness scores from the barrel cortex were normalized by dividing the luminance values from the underlying white matter to give a final brightness ratio. Thus, a final brightness ratio of "1.0" would represent a barrel cortex with no staining and higher brightness value, representing fewer PNNs.

2.5. Diffraction measurements

We used a custom-built transmission-mode diffractometer (Lazarev et al.,2023) comprising a Xenocs source, Genix 3D Cu with Fox 12-53 Cu Mirror (λ = 0.1540562 nm), an Advacam MiniPIX TPX3 detector (256x256 pixel sensor array, with the pixel size of 55 μm^2), and a sample stage. The image is shown in Fig. 1(a). The collimated beam had an approximate spot size of 1 mm diameter. The diffractometer was calibrated using a sample of powdered silver behenate. The samples were scanned for 2 minutes at 20 mm sample-to-detector distance. Measurement data was saved as an array of 256x256 integers. A typical diffraction pattern is shown in Fig. 1(b).

2.6. Data analysis

Each diffraction image is digitally represented as a 256x256 matrix. As the first step, the faulty pixels are removed. Next, azimuthal integration can be performed, and the scattered intensity becomes the function of the distance to the center. This distance can be converted to the

momentum transfer, q. The bright concentric rings of Fig. 1(b) appear as peaks in this dependence. In simple, straightforward cases, the position and amplitude of these peaks provide enough information for classifications. However, for complex situations, more advanced machine-learning methods are needed.

For this work, we developed an approach based on the two-dimensional Fourier transformation (2DFT). When 2DFT is performed, the 256x256 matrices of the Fourier coefficients are obtained for each image. To eliminate the contribution of the primary beam, the auxiliary matrices are constructed with zeroes everywhere except the locations of the bright circles. 2DFT of these matrices contain the Fourier coefficients of the primary beam images. The difference between 2DFTs of original and auxiliary matrices provides the Fourier coefficients associated only with the tissue. The elements of the obtained matrices are normalized by the element at (0,0), i.e., brightness, to exclude the irregularities produced by fluctuations in the exposure times and material densities. Next, standard scaling is used to prevent arbitrary pixels from having too much weight. It is achieved by the division of each element of specific arrays by the corresponding element of the total mean matrix.

In the following step, a procedure similar to face recognition (eigenface) (Sirovich & Kirby, 1987; Turk & Pentland, 1991) is accomplished. Each of 28 (256x256) arrays of Fourier coefficients is flattened, i.e., it is represented as a row with 65,536 elements. For the resulting 65,536x28 matrix, a principal component (PC) analysis is performed. Accordingly, each sample is described as a point in the PC space.

3. Results

3.1. PNN staining results

In previous work, we found that layer 4 (L4) of the barrel cortex houses the greatest quantity of PNNs (Chu et al., 2018). We also found that whisker-trimming affects PNNs most significantly within L4 of the barrel cortex (McRae et al., 2007). Therefore, we focused our analysis specifically on this layer. Current results confirm previous findings. Whisker-trimming resulted in a significant reduction of L4 barrel cortex PNNs in TW mice when compared with Control mice (see Fig. 2(a,b) for representative samples). The average brightness ratio for Control vs. TW mice was 0.56 and 0.62 respectively, ($p=0.025$) (see Fig. 2(c)). Trimming resulted in an approximate 10% increase in brightness.

3.2. Analysis of diffraction patterns

To determine if changes in PNN density were correlated with changes in the fine structure of the slices as measured by the diffractometer, we measured the X-ray diffraction patterns for each of the 28 samples. The typical result is shown in Fig. 1(b), exhibiting three bright concentric rings. Visually, the patterns of the Control mice and those with trimmed whiskers cannot be distinguished. After azimuthal integration and unit conversion, the intensity can be plotted as a function of the momentum transfer magnitude, Fig. 3(a). Three peaks are identified, approximately at 4, 9.5, and 13.2 inverse nanometers, which correspond to the structural periodicities of 1.54, 0.65, and 0.46 nm, respectively. There is also an amorphous scattering signal at small q, which obeys Porod's Law (Porod, 1951), i.e., it is proportional to inverse q in the fourth power.

One can see that the Control and TW dependencies are not different, with almost the same peak positions for all the curves and the peak magnitudes unrelated to the specifications. As can be further seen in Fig. 3(b), for the mean curves, the only difference can be seen at small q where the amorphous scattering dominates. The stronger signal from the sensory deprived mice supports our conclusion below that these mice do not develop the same brain structure as untrimmed Control mice. We developed and performed the advanced machine-learning-based procedure described in Section 2.6. The explained variances for the determined principal components are shown in Table 1.

Table 1. Explained variance for the first ten dimensions of the principal component analyses (PCA).

PC0	**PC1**	**PC2**	**PC3**	**PC4**	**PC5**	**PC6**	**PC7**	**PC8**	**PC9**
56.86%	13.12%	6.62%	3.69%	2.81%	2.55%	2.617%	1.9%	1.77%	1.26%

The results in the 3D and 2D PC spaces are presented in Fig. 4.

Figure 4 demonstrates that the clusters of the Control mice and the TW mice are well separated, with only one blue point (TW) having a positive PC2 value and only two red points (Control) having negative PC2 values. Blue points are concentrated near zero along the PC1 axis, while most red points have large values (positive or negative). We interpret this as a formation of structures at the nanoscale in Control mice, while these structures are not formed in the mice with trimmed whiskers deprived of sensory information.

4. Discussions

Our current results confirm previous studies that have demonstrated that sensory deprivation via whisker-trimming reduces perineuronal nets in the mouse barrel cortex, as demonstrated by immunohistochemistry (IHC) (McRae et al., 2007). Here, in a novel approach, we attempt to reveal the origin of these changes on a molecular level. We employ the X-ray diffraction (XRD) technique and show that this approach can be used on brain tissue to detect structural changes. Isolated barrel cortices from mice that had either undergone 30 days of whisker-trimming or simple handling (controls) were subjected to x-ray diffraction analysis. The characteristic peaks related to molecular periodicities of 1.54, 0.65, and 0.46 nm were determined for all samples, with the control and trimmed-whiskers ones being indistinguishable. However, after a specifically developed advanced analysis based on the 2D Fourier transformation of XRD images and the face recognition procedure in the reciprocal space, the control and trimmed-whiskers groups form distinct clusters in principal component space. This demonstrates that the brains of these two groups have different structures, both at physiological (Chu et al., 2018) and molecular levels. All the samples obtained from the mice with trimmed whiskers have much smaller values of one of the principal components in the reciprocal space, indicating the lack of corresponding molecular structure. We argue that such a lack of structure is because of sensory deprivation.

While the individual building blocks of PNNs are well known, there is little literature on the periodicity of PNNs as a complete structure and its molecular origin. However, it has already been mentioned that X-ray scattering has been successfully used to examine differences between pathological and healthy breast tissue by focusing on structural changes in collagen fibrils (Conceicao et al., 2019). And Landahl et al. (2011), using an X-ray diffraction microprobe, were able to gather data on the periodic structure of tau tangles in brain tissue (Landahl et al., 2011). It is likely that our results are similarly reporting changes to periodic structures within the barrel cortex. Given the changes to PNNs demonstrated through IHC, we suggest that the changes of the diffraction patterns reported here are related to alterations in the PNNs. Functionally, PNNs are thought to physically protect neuronal synapses from damage by creating a barrier around them (Li et al., 2024; Cabungcal et al., 2013) Chondroitin sulphate proteoglycans (CSPGs) make up the bulk of PNNs, and these are bound together with link proteins, tenascin-r, and hyaluronidase to give PNNs their distinct and repetitive lattice-like macrostructure. These structures were partially eliminated after trimming (See Fig. 2), and this is likely related to the changes in diffraction patterns.

PNNs are also thought to protect against oxidative stress by binding positively charged metal ions (Li et al., 2024; Cabungcal et al., 2013). It is their unique structure which allows them to do this. CSPGs contain glycosaminoglycan side chains (GAGs) surrounding a core protein (aggrecan, brevican, etc.), and these are conformed to allow anionic binding sites to attract metal cations away from the neurons they surround (Soleman et al., 2013; Morawski et al., 2015). GAGs are bound across the core CSPG protein, at upward of 100 GAGs at regular/semi-regular intervals (Kiani et al., 2002). It is these chains specifically which have been reportedly dissolved in Alzheimer's disease (Logsdon et al., 2022). WFA, lectin used for visualizing PNNs herein, specifically binds to GAGs, and loss of visible nets reported here may correspond specifically to reduction in GAGs.

Currently, our methodology describes a novel technique for examining in-vitro tissue to determine changes in molecular structure related to alternations of PNNs. It is feasible to think that this could lead to in-vivo use, where X-ray diffraction becomes a useful diagnostic tool. It has been shown that Alzheimer's affects PNN distribution; schizophrenia, chronic pain, and other pathologies have also been seen to alter PNNs, in a region-specific manner (Mauney et al., 2013; Tansley et al., 2022; Bitanihirwe & Woo, 2014). As we gain better understanding of exactly how the PNN is affected, and the timing of disruptions to the PNN, it is likely that we will be able to hone this technique further, for more direct and accurate measurements. Additional studies are needed to connect our current observations and the actual molecular content of brain tissue. Deeper investigation is necessary to determine the relations between nanoscale changes in molecular structures and the microscale changes observed in PNNs post-sensory deprivation and pathology. The XRD method is also quicker than using IHC, reducing time sectioning, staining, and visualizing tissue. This could be extremely valuable when processing large sample quantities.

References:

1. Bitanihirwe, B. K., & Woo, T. U. (2014). Perineuronal nets and schizophrenia: The importance of neuronal coatings. *Neuroscience and Biobehavioral Reviews, 45*, 85–99. https://doi.org/10.1016/j.neubiorev.2014.03.018
2. Bragg, W. L. (1914). The analysis of crystals by the X-ray spectrometer. *Proceedings of the Royal Society of London, 89*(A), 468.
3. Cabungcal, J. H., Steullet, P., Morishita, H., Kraftsik, R., Cuenod, M., Hensch, T. K., & Do, K. Q. (2013). Perineuronal nets protect fast-spiking interneurons against oxidative stress. *Proceedings of the National Academy of Sciences of the United States of America, 110*(22), 9130-9135. https://doi.org/10.1073/pnas.1300454110
4. Chu, P., Abraham, R., Budhu, K., Khan, U., De Marco Garcia, N., Brumberg, J. C. (2018). The impact of perineuronal net digestion using chondroitinase ABC on the intrinsic physiology of cortical neurons. *Neuroscience, 388*, 23–35. https://doi.org/10.1016/j.neuroscience.2018.07.004
5. Conceicao, A. L. C., Antoniassi, M., & Poletti, M. E. (2010). Assessment of the differential linear coherent scattering coefficient of biological samples. *Nuclear Instruments and Methods in Physics Research, A, 619*, 67–70. https://doi.org/10.1016/j.nima.2009.12.021
6. Conceicao, A. L. C., Meehan, K., Antoniassi, M., Piacenti-Silva, M., & Poletti, M. E. (2019). The influence of hydration on the architectural rearrangement of normal and neoplastic human breast tissues. *Heliyon, 5*(2), e01219. https://doi.org/10.1016/j.heliyon.2019.e01219
7. Crapser, J. D., Spangenberg, E. E., Barahona, R. A., Arreola, M. A., Hohsfield, L. A., & Green, K. N. (2020). Microglia facilitate loss of perineuronal nets in the Alzheimer's disease brain. *EBioMedicine, 58*, 102919. https://doi.org/10.1016/j.ebiom.2020.102919
8. Cunha, D. M., Oliveira, O. R., Pérez, C. A., & Poletti, M. E. (2006). X-ray scattering profiles of some normal and malignant human breast tissues. *X-ray Spectrometry, 35*, 370-374. https://doi.org/10.1002/xrs.921
9. Denisov, S., Blinchevsky, B., Friedman, J., Gerbelli, B., Ajeer, A., Adams, L., Greenwood, C., Rogers, K., Mourokh, L., & Lazarev, P. (2024). Vitacrystallography: Structural biomarkers of breast cancer obtained by X-ray scattering. *Cancers, 16*(24), 2499. https://doi.org/10.3390/cancers16142499
10. Härtig, W., Brauer, K., & Brückner, G. (1992). Wisteria floribunda agglutinin-labelled nets surround parvalbumin-containing neurons. *Neuroreport, 3*(10), 869–872. https://doi.org/10.1097/00001756199210000-00012
11. Hijazi, S., Smit, A. B., & van Kesteren, R. E. (2023). Fast-spiking parvalbumin-positive interneurons in brain physiology and Alzheimer's disease. *Molecular Psychiatry, 28*, 4954–4967. https://doi.org/10.1038/s41380-023-02168-y
12. Higgins, M. K., & Lea, S. M. (2017). On the state of crystallography at the dawn of the electron microscopy revolution. *Current Opinion in Structural Biology, 46*, 95–101. https://doi.org/10.1016/j.sbi.2017.06.005
13. Kiani, C., Chen, L., Wu, Y. J., Yee, A. J., & Yang, B. B. (2002). Structure and function of aggrecan. *Cell Research, 12*(1), 19–32. https://doi.org/10.1038/sj.cr.7290106
14. Kidane, G., Speller, R. D., Royle, G. J., & Hanby, A. M. (1999). X-ray scatter signatures for normal and neoplastic breast tissues. *Physics in Medicine and Biology, 44*(7), 1791-1802. https://doi.org/10.1088/0031-9155/44/7/316

15. Landahl, E. C., Antipova, O., Bongaarts, A., Barrea, R., Berry, R., Binder, L. I., Irving, T., Orgel, J., Vana, L., & Rice, S. E. (2011). X-ray diffraction from intact tau aggregates in human brain tissue. *Nuclear Instruments and Methods in Physics Research, Section A, 649*(1), 184–187. https://doi.org/10.1016/j.nima.2011.01.059
16. Lazarev, A. P., Lazarev, P. I., & Yuk, D. T. W. (2023) Alpha diffractometer that does not employ a beam stopper (Patent No. US20230341339).
17. Li, X., Wu, X., Lu, T., Kuang, C., Si, Y., Zheng, W., Li, Z., & Xue, Y. (2024). Perineuronal nets in the CNS: Architects of memory and potential therapeutic targets in neuropsychiatric disorders. *International Journal of Molecular Sciences, 25*, 3412. https://doi.org/10.3390/ijms25063412
18. Logsdon, A. F., Francis, K. L., Richardson, N. E., Hu, S. J., Faber, C. L., Phan, B. A., Nguyen, V., Setthavongsack, N., Banks, W. A., Woltjer, R. L., Keene, C. D., Latimer, C. S., Schwartz, M. W., Scarlett, J. M., & Alonge, K. M. (2022). Decoding perineuronal net glycan sulfation patterns in the Alzheimer's disease brain. *Alzheimer's & Dementia: The Journal of the Alzheimer's Association, 18*(5), 942–954. https://doi.org/10.1002/alz.12451
19. Mauney, S. A., Athanas, K. M., Pantazopoulos, H., Shaskan, N., Passeri, E., Berretta, S., & Woo, T.-U. W. (2013). Developmental pattern of perineuronal nets in the human prefrontal cortex and their deficit in schizophrenia. *Biological Psychiatry, 74*(6), 427–435. https://doi.org/10.1016/j.biopsych.2013.05.007
20. McRae, P. A., Rocco, M. M., Kelly, G., Brumberg, J. C., & Matthews, R. T. (2007). Sensory deprivation alters aggrecan and perineuronal net expression in the mouse barrel cortex. *Journal of Neuroscience, 27*(20), 5405-5413. https://doi.org/10.1523/JNEUROSCI.5425-06.2007
21. Morawski, M., Reinert, T., Meyer-Klaucke, W., Wagner, F. E., Tröger, W., Reinert, A., Jäger, C., Brückner, G., & Arendt, T. (2015). Ion exchanger in the brain: Quantitative analysis of perineuronally fixed anionic binding sites suggests diffusion barriers with ion sorting properties. *Scientific Reports, 5*, 16471. https://doi.org/10.1038/srep16471
22. Paxinos, G., & Franklin, K. B. (2019). *Paxinos and Franklin's the mouse brain in stereotaxic coordinates* (5th ed.). Academic Press.
23. Pizzorusso, T., Medini, P., Berardi, N., Chierzi, S., Fawcett, J. W., & Maffei, L. (2002). Reactivation of ocular dominance plasticity in the adult visual cortex. *Science, 298*(5596), 1248-1251. https://doi.org/10.1126/science.1072699
24. Porod, G. (1951). Die Röntgenkleinwinkelstreuung von dichtgepackten kolloiden Systemen. *Kolloid-Zeitschrift, 124*, 83–114.
25. Shi, Y. A. (2014). Glimpse of structural biology through X-ray crystallography. *Cell, 159*(5), 995-1014. https://doi.org/10.1016/j.cell.2014.10.051
26. Sirovich, L., & Kirby, M. (1987). Low-dimensional procedure for the characterization of human faces. *Journal of the Optical Society of America A, 4*(3), 519–524. https://doi.org/10.1364/JOSAA.4.000519
27. Soleman, S., Filippov, M. A., Dityatev, A., & Fawcett, J. W. (2013). Targeting the neural extracellular matrix in neurological disorders. *Neuroscience, 253*, 194–213. https://doi.org/10.1016/j.neuroscience.2013.08.050
28. Suttkus, A., Morawski, M., & Arendt, T. (2016). Protective properties of neural extracellular matrix. *Molecular Neurobiology, 53*, 73–82. https://doi.org/10.1007/s12035-014-8990-4

29. Tansley, S., Gu, N., Guzmán, A. U., Cai, W., Wong, C., Lister, K. C., Muñoz-Pino, E., Yousefpour, N., Roome, R. B., Heal, J., Wu, N., Castonguay, A., Lean, G., Muir, E. M., Kania, A., Prager-Khoutorsky, M., Zhang, J., Gkogkas, C. G., Fawcett, J. W., Diatchenko, L., Ribeiro-da-Silva, F., De Koninck, Y., Mogil, J., & Khoutorsky, A. (2022). Microglia mediated degradation of perineuronal nets promotes pain. *Science, 377*(6601), 80-86. https://doi.org/10.1126/science.abl6773
30. Turk, M., & Pentland, A. P. (1991). Face recognition using eigenfaces. In *Proceedings of the IEEE Conference on Computer Vision and Pattern Recognition* (pp. 586-591). Maui, HI, USA. https://doi.org/10.1109/cvpr.1991.139758
31. Worthington, C., & Tomlin, S. (1955). Small-angle X-ray diffraction patterns of collagen. *Nature, 175*, 811.

Acknowledgements: This work was supported by NIGMS 122657 to JCB.

Figure Legends

Figure 1. (a) Diffractometer. (b) The X-ray diffraction pattern produced by the sample containing a mouse brain slice (2.4 x 1.75 x 1 mm). The bright circle is the unscattered image of the primary beam. The bright concentric rings are associated with constructive interference of light scattered by periodically structured material. The black point near the center is a faulty pixel.

Figure 2. Representative PNN staining of barrel cortex for (a) control and (b) trimmed (TW) mice. Outlines indicate barrel cortex for each sample. (c) Quantification of brightness within layer IV. Mice whose whiskers have been trimmed show higher brightness scores compared with control mice. Bars represent population means and error bars are indicative of one standard error of the mean, N's are reflective of number of samples.

Figure 3. (a) Dependencies of the scattered intensity on the momentum transfer magnitude for all measured samples and (b) for the mean curves, with the Control and TW shown in red and blue, respectively.

Figure 4. (a) The PCA-transformed data with the 3D PC space. (b) The 2D PC space. The red and blue points are associated with the Control mice and those with trimmed whiskers, respectively.

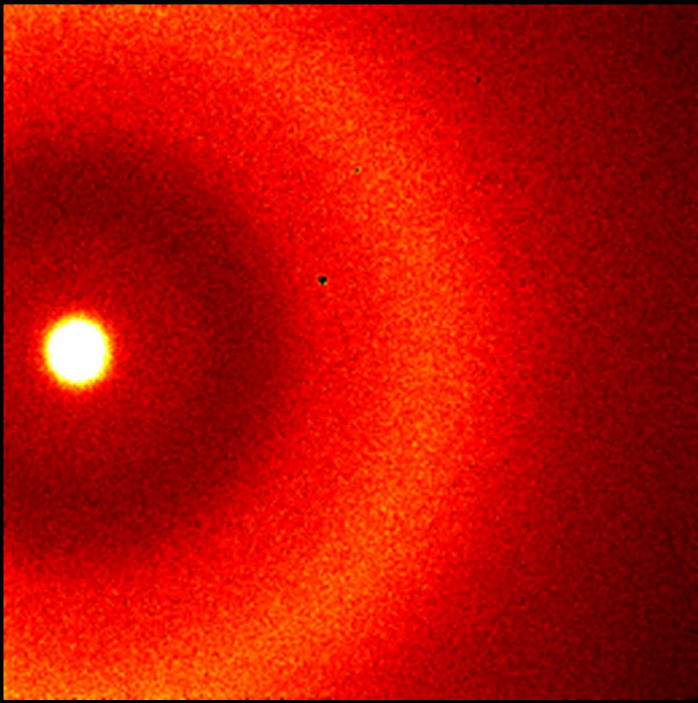

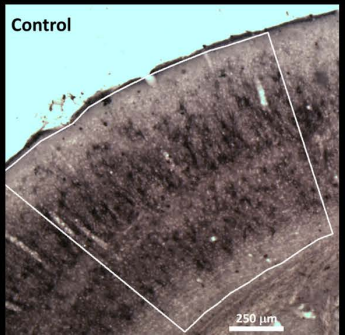
Control
250 µm

Trimmed Whiskers

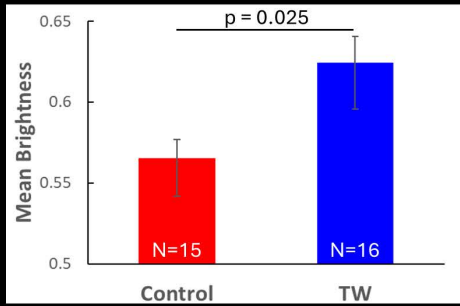
p = 0.025
Mean Brightness
0.65
0.6
0.55
0.5
N=15
N=16
Control
TW

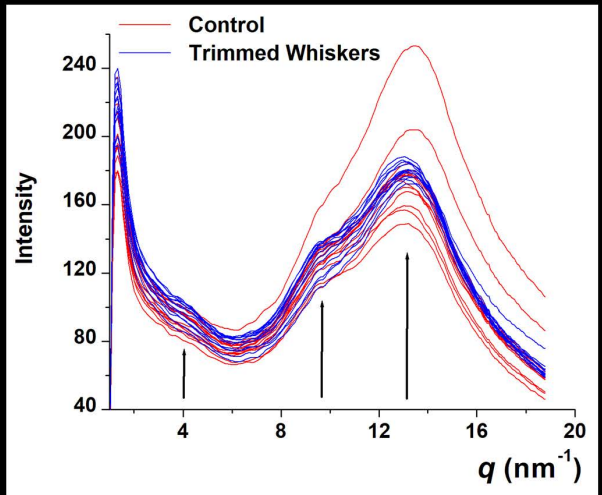
Control
Trimmed Whiskers
Intensity
240
200
160
120
80
40
4
8
12
16
20
q (nm-1)

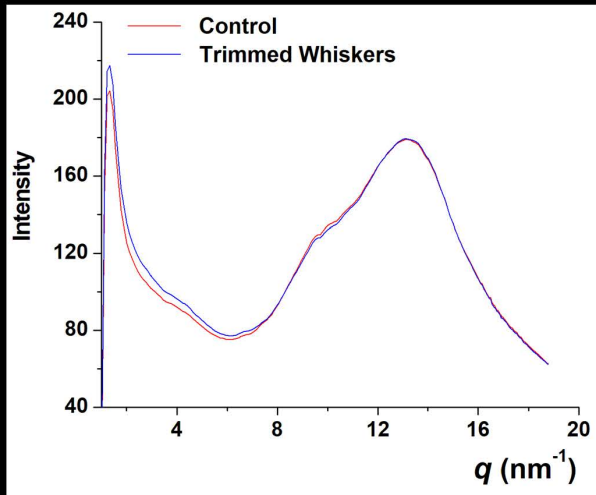
Control
Trimmed Whiskers
Intensity
240
200
160
120
80
40
4
8
12
16
20
q (nm-1)

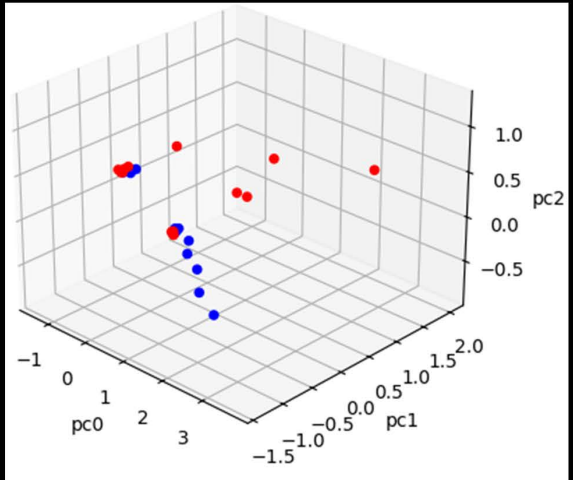
pc0
pc1
pc2

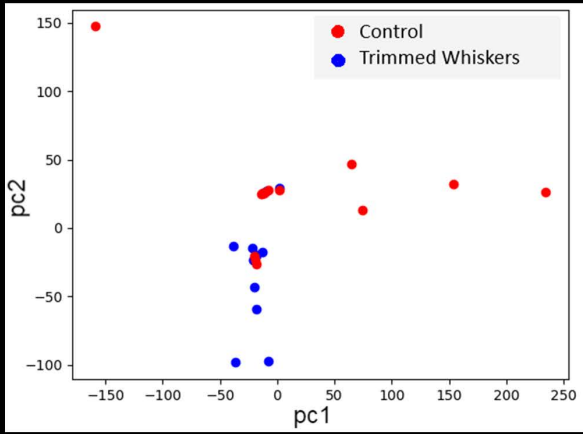
Control
Trimmed Whiskers
pc1
pc2